The Structural Evolution and Densification Mechanisms of Nanophase Separation Sintering

Citation: Oliver, C., Schuh, C.A. The Structural Evolution and Densification Mechanisms of Nanophase Separation Sintering. Metall Mater Trans A 52, 4946–4956 (2021).

As Published: https://doi.org/10.1007/s11661-021-06437-9

Publisher: Springer Science and Business Media LLC

Persistent URL: https://hdl.handle.net/1721.1/132937

Version: Author's final manuscript: final author's manuscript post peer review, without publisher's formatting or copy editing

The Structural Evolution and Densification Mechanisms of Nanophase Separation Sintering

The Structural Evolution and Densification Mechanisms of Nanophase Separation Sintering

Christian Oliver
Cambridge, MA, 02139
coliver@mit.edu
Massachusetts Institute of Technology

Christopher A. Schuh
Cambridge, MA, 02139
schuh@mit.edu
Massachusetts Institute of Technology

1

Abstract

Nanophase separation sintering (NPSS) facilitates low temperature, pressureless sintering through the formation of solid phase necks driven by phase separation. Systems that have been shown to exhibit this phenomenon are W-Cr, Cr-Ni and to a lesser degree Ti-Mg. Initial information on the average rate-limiting sintering kinetics in these systems was obtained using traditional master sintering curve analysis, but it is very clear that multiple processes occur during NPSS, and these should each have their own characteristic kinetics. Here we analyze these three systems in greater kinetic detail using densification rates in a Kissinger-style analysis derived explicitly for densification data. For the W-Cr and Cr-Ni systems two critical temperatures were identified: one at low temperatures for the formation of the secondary phase necks, and a second one at high temperatures corresponding to the onset of rapid densification. The activation energies of these processes are different, and reflective of bulk solute diffusion and interdiffusion, respectively. Combined with microstructural observations, these data show that the onset of rapid densification at high temperatures is facilitated by the presence of the second-phase necks, and occurs at the point where the system can fully interdiffuse, rehomogenizing those necks. These observations help explain why the Ti-Mg system does not densify well, because it does not exhibit redissolution at high temperatures. These results help clarify the conditions needed to achieve NPSS and may support design of new alloys for NPSS behavior.

I - Introduction

Nanophase separation sintering (NPSS) is a sintering method that allows for low homologous temperature, pressureless sintering of some specific alloy systems. Park[1] first demonstrated NPSS in the W-Cr system, obtaining samples with near full relative density at temperatures well below 50% the melting temperature of tungsten, and with zero applied pressure[1,2]. Park elaborated the structural

evolution leading to this rapid densification, which was enabled by the unique starting state of the powders: nanocrystalline with a grain size of ~10 nm, and containing a supersaturation of 5-15 at% dissolved Cr. Upon heating, a chromium phase began to separate from solution with tungsten, preferentially segregating to particle surfaces and forming interparticle necks at temperatures as low as 950 °C. These necks were proposed to facilitate rapid diffusion of the tungsten through the neck to fill pores and densify the material. This general pathway (second phase precipitation facilitating more rapid mass transport) is conceptually similar to what happens in liquid phase sintering and supersolidus liquid phase sintering [3–10], but importantly, in NPSS all of this structural evolution occurs completely in the solid state. NPSS therefore avoids the slumping that can occur in some liquid phase sintering systems, and can be used to free-sinter complex green geometries[11–14]. This provides an advantage to additive manufacturing techniques such as binder jet printing, by maintaing high dimensional tolerences of the as-printed geometry[13,15,16]. The applicability of NPSS to both traditional and additive near net shape processes can make it desirable for many applicatons such as medical and areospace[15,17].

After identifying the structural evolution pathway in NPSS, Park proposed a set of criteria for a binary material system that would potentially exhibit it [1,2]:

i. The base element and the secondary element should exhibit a phase separation in equilibrium at the desired composition,
ii. the secondary element should exhibit a lower surface energy than the base element, facilitating surface segregation and neck formation when the phase separation takes place and
iii. the secondary phase should have a relatively high solubility of the base element at the sintering temperature, the better to facilitate transport by diffusion.

3

Beyond these features for the material system, it is also necessary that the initial powder be nanocrystalline and supersaturated with the secondary element. It is only in a supersaturated condition that phase separation can occur upon heating, and the nanocrystalline structure facilitates rapid low-temperature mass transport to particle surfaces in order to construct necks.

Since the first report of Park, NPSS has been subsequently reported in two additional systems. First, the Cr-Ni system meets all of the criteria for NPSS using nickel to enhance the sintering of chromium[2]. Sintering experiments in this system exhibited similar densification reported for the W-Cr system, with early phase separation and neck formation preceding the largest densification. Furthermore, experiments in this system involved more rapid grain coarsening, and consequently illustrated that a nanocrystalline structure was not necessary during the entire sintering process, only for the initial neck formation[2]. Second, the Ti-Mg system was explored as a test of the three Park criteria (i-iii) above, because it met the first two but not the third. This system exhibited neck formation and densification at temperatures below 50% the melting point of titanium[18]. However, unlike the W-Cr and Cr-Ni systems, the Ti-Mg samples did not achieve near full density without an artificially high green density produced by cold pressing at very high pressures; this is perhaps because the system lacked the high solubility of Ti in Mg, as stipulated by the third Park criterion.

These three systems (W-Cr, Cr-Ni, Ti-Mg) are all rather different thermodynamically, and satisfy the Park criteria above to varying degrees. They all exhibit more rapid densification kinetics than nominally expected for conventional densification processes. However, only a single method has so far been used to assess the kinetics of NPSS in all these systems: the master sintering curve (MSC) technique with constant heating rate experiments[19–25]. The guiding principle of MSC analysis is that the geometric parameters of the sintering process and the thermal history of the sintered pellet are independent of each other for a given powder [19]. This is tantamount to assuming that the dominant mechanism that defines the sintering process will not be different for a particular powder (material,

4

particle size distribution, etc.) no matter the thermal processing applied. In the above studies on NPSS, this technique was used to establish lower-than-expected activation energies for sintering, illustrating that densification was indeed kinetically dominated by a low-energy rapid transport mechanism consistent with the formation of the second phase necks. However, MSC analysis heavily weights the mechanism that results in the majority of densification and could miss other necessary and important stages of the sintering process[19,26–28], of which there are clearly several in NPSS, including the phase separation and assmebly of necks, and later rapid densification. While MSC analysis has established an average rapid kinetic singature for NPSS, these stages require further elaboration.

Therefore, the purpose of this research is to present additional kinetic analysis of NPSS, to better separate the critical processes that occur at various temperatures and times. Such results provide insight on the necessary conditions of NPSS proposed by Park[1,2], and foreshadow the optimization of temperature-time cycles for such systems.

II - Data and Experiments

This paper analyzes sintering data from all three previously reported NPSS systems: W-Cr[1], Cr-Ni [2], and Ti-Mg[18]. We make use of raw data from those original studies and analyze that data in new ways. In each case, we denote the composition in atomic percentages, and the following specific compositions are considered here: W-15Cr, Cr-5Ni, Cr-10Ni, Cr-15Ni, and Ti-20Mg.

Additionally, new corroborating experiments are conducted on W-15Cr, following procedures generally consistent with the original reference. For those experiments, we prepared initial powders through a process of high energy milling using elemental powders of 99.9% W and 99.2% Cr from Alfa Aesar. The powders are were milled with a SPEX 8000M shaker mill in a Tungsten Carbide vial with tungsten carbide milling media, in a glove box under ultra-high purity argon. The milling media to

5

powder ratio was 5:1, and ethanol was used as a process control agent. The powder was milled for 20 hr, which is a condition that achieves both supersaturation and nanocrystallinity[1]. Green bodies with a diameter of 6 mm and a height of ~3 mm were pressed uniaxially with a pressure of ~400 MPa. The production of these samples is in accordance with the uniaxial die pressing specifications of ASTM B925 and the dimensions of the samples are within the specifications of ASTM E831 for dilatometry[29,30].

Sintering experiments were performed in a mode of constant heating rate in a dilatometer, specifically a Netzsch 402-F3 Hyperion Thermal Mechanical Analyzer. Those data are provided as the height of a pressed and sintered compact, measured as a function of temperature during a constant heating rate experiment. Assuming isotropic shrinkage, the relative change in densification can be calculated for each heating rate tested, and validated against the final sample dimensions and density.

Imaging was performed on a FEI Helios 600 scanning electron microscope (SEM). Some samples were partially sintered in order to observe intermediate sintering structures. These samples were processed in a similar manner to the other specimens described above, similarly heated at a constant rate to a target temperature, but then gas quenched for observation. Such partially sintered samples were mechanically broken so that the internal powder structure could be observed. Fully densified samples were mounted in epoxy and polished to a finish of 0.05 μm for standard metallographic observation of the grain structure. Backscattered imaging in the SEM was primarily used to observe the chemical difference in the phases involved. X-ray Diffraction used to confirm phase formation was performed using a Panalytical X'Pert Pro diffractometer with Cu-Kα radiation at 45 kV and 40 mA.

III - The W-Cr system

6

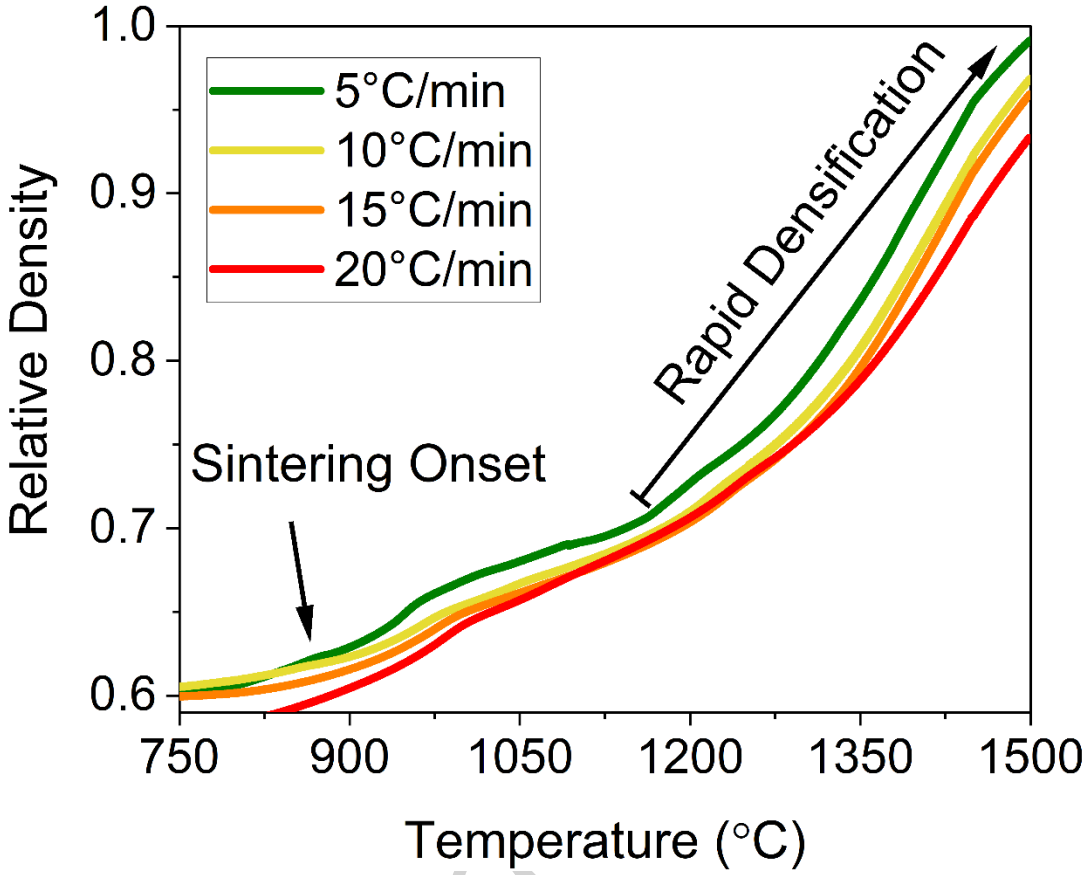

Figure 1: Relative density for W-15Cr samples sintered at heating rates of 5, 10, 15, and 20 °C/min

The newly-collected raw data for the W-15Cr system is shown in Fig. 1. The previous report on the W-Cr system by Park et al. obtained data demonstrating the same trends[1]. Minor differences in initial densities are representative of variations in milling and pressing. What is important to note about Fig. 1 is the uptick in densification starting at around 900°C, and continuing to the maximum test temperature of 1550°C; this is a temperature range where W does not sinter at all, and pure Cr only barely begins to densify (by perhaps 5%)[1,31]. In contrast, NPSS as in Fig. 1 achieves >90% density tungsten at temperatures below 50% of the melting temperature of tungsten without the use of a liquid phase. In some cases here and in Ref. [1], near full densities of ~95-98% are obtained, in every case

7

without applied pressure (the contact pressure from the dilatometer is a negligible 0.003 MPa) and without substantial isothermal holds. The four different rates in Fig. 1 also show the expected kinetic effects whereby longer time-at-temperature (lower scan rates) leads to higher densification.

In order to gain an understanding of the mechanisms facilitating the densification of these materials, a master sintering curve analysis was first performed. The thermal history of a sintering process is given by:

$$\theta\big(t,T(t)\big) = \int_0^t \frac{1}{T} e^{-\frac{Q}{RT}} dt \qquad (1)$$

where t is time, T is temperature, Q is the controlling activation energy of the sintering process and R is the universal gas constant [19]. The premise of the MSC is that if the activation energy of the dominant sintering process is known, the densification of a material can be predicted for any given heating profile, as long as that sintering process dominates over the entire sintering range examined. If different thermal histories are applied, they all collapse onto a single master curve when normalized by Eq. (1) with the correct activation energy. By seeking such a collapse, MSC analysis can also be used to best-fit the activation energy. In practice, the best-fit activation energy is the one where the mean residual square error between different heating profiles become minimized. Since this sintering process is both pressureless and absent of any electrical or magnetic fields, a process like MSC where only the thermal work applied to the system is varied is an optimal way to determine the kinetic parameters of sintering mechanisms.

This type of MSC analysis was used by Park et al.[1] using data similar to those in Fig. 1, to return an activation energy for the mechanically alloyed W-15Cr system as ~373 kJ/mol. In Fig. 2 we repeat this standard analysis using newly collected data in Fig. 1. By assuming a test value of the activation energy,

8

calculating the mean square residual error among the four heating rates tested, and then changing the test value and repeating, we attain results such as, those shown in Fig. 2a. The value of 376 kJ/mol captures the overall densification kinetics best of the three examples shown, and in Fig. 2b a high-resolution map across activation energy space confirms that this is the activation energy achieving the lowest residual error.

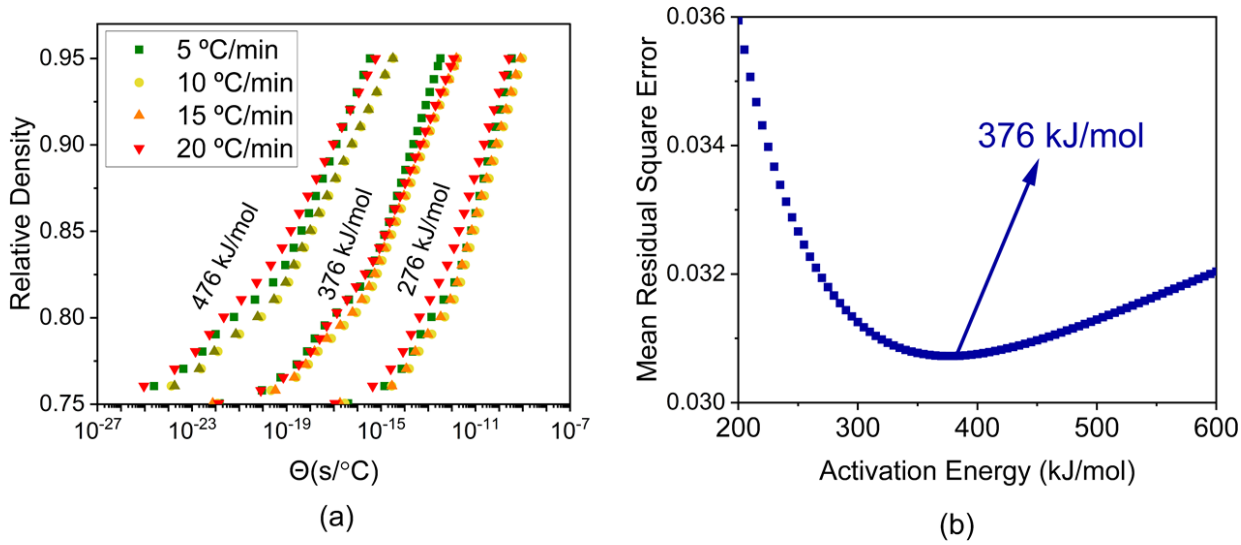

Figure 2: Master sintering curve analysis for W-15Cr. The first figure shows the overlap of the θ parameters at different activation energies illustrating how 376 kJ/mol presents a best fit. The second graph is of the Mean Residual Square Error of the fit for different activation energies showing a minimum at 376 kJ/mol.

MSC theory expects that the densification curve will be smooth and easily represented with a single activation energy. However, we know that the processes involved in NPSS are complex, involving phase separation, substantial structure change of the powder and inter-particle necks, densification, and possibly other diffusional reactions such as redissolution of solute or coarsening of second phases. And indeed, close inspection of Fig. 1 (and prior published data on NPSS under fixed heating rate conditions) reveals that the densification curves have a series of fluctuations and inflection points. Note, for example, the consistent small 'bump' in the curves of Fig. 1 at around 1000-1100° C. In order to amplify

9

such inflections, it is useful to take the first derivative of the densification curve with respect to time, providing densification rate information. An example of such an analysis is provided for a W-15Cr sample heated at 15°C/min in Figure 3; the curve now reveals a sequence of characteristic densification events, which can be analyzed structurally and kinetically in their own right. In what follows we investigate these in turn.

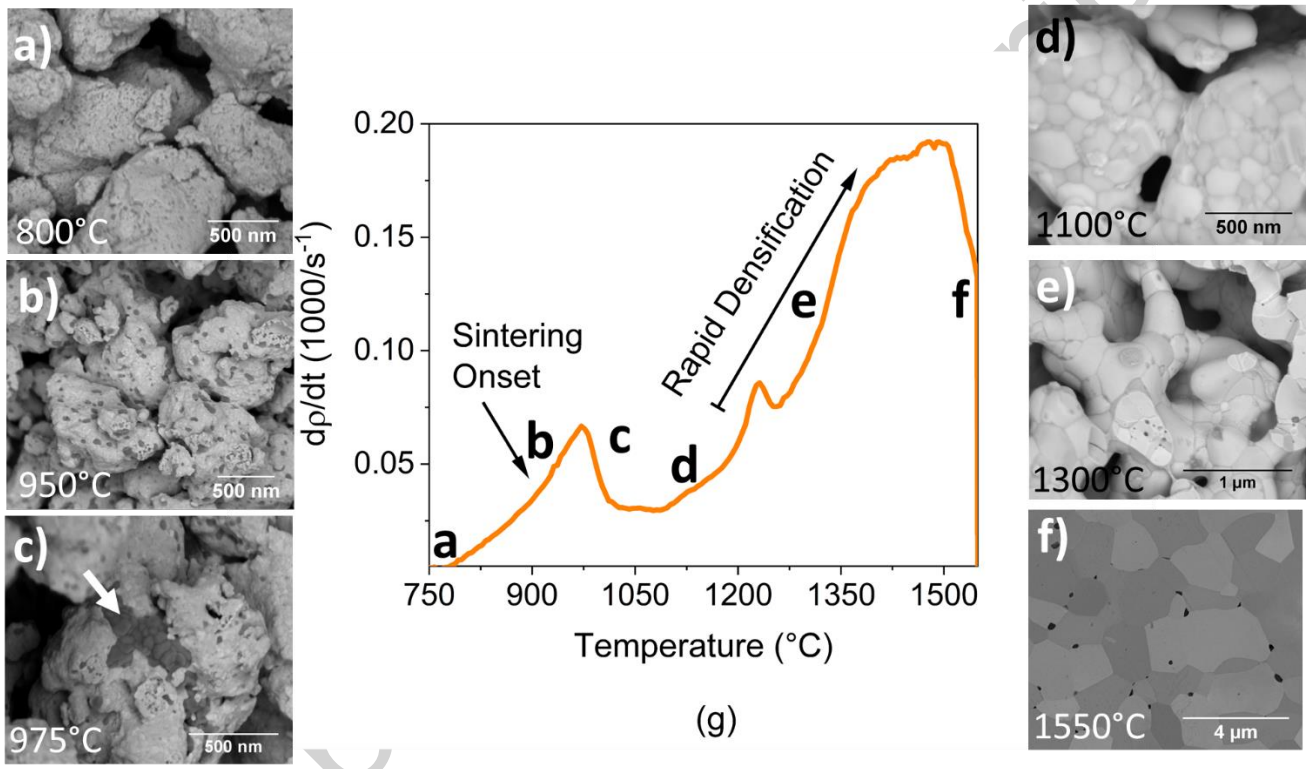

Figure 3: Images of samples quenched at different temperatures during the densification process (a) – (f) and the densification rate curve for W15Cr heated at 15°C/min (g) including the relative positioning of the samples on the curve.

First, we observe a substantial peak that occurs between 950 and 1000°C. This peak is associated with the phase separation of Cr from W, and the formation of interparticle necks between particles as a result of that phase separation. We may visualize these changes using a series of SEM images taken from samples subjected to interrupted sintering runs and quenched at intermediate temperatures. As shown in Fig. 3a, at 800°C we can just begin to observe the onset of phase separation,

10

as seen by the very small dark second phase that appears to speckle the surface of the powder particles. As the temperature rises, this second phase becomes more prominent in both volume fraction and size: at 950° C the powder particles are convincingly spotted with small grains of Cr on their surfaces as seen in Fig. 3b. Finally, at 1000°C, we see the aggregation of the second phase into large particle-spanning necks as denoted by the arrow in Fig. 3c. Because Fig. 3 presents densification data, this peak does not show the exact temperature at which we first see phase separation. However, the image at 800°C helps to confirm that this first peak represents the onset of the initial stage of sintering in the system.

To verify that the secondary phase that presents itself in Fig 3b and Fig 3c is in fact a Cr rich phase, XRD was performed on both of these and compared with that of both as ball milled powder and the sample quenched at 800 °C (Fig 3a). For both the as milled powder and the sample quenched at 800 °C, the Cr phase could not be detected. This indicates that the small amount of the Cr phase seen in the 800 °C sample is below the threshold for XRD. The samples quenched at 950 °C and 975 °C, however, had a distinct signal from the Cr phase. Using the integrated intensities for the primary peaks in these samples gives an estimated Cr fraction of 5-8 vol% for these samples.

Thus, the first densification peak is associated with the unique NPSS behavior whereby phase separation leads to interparticle necks and some amount of rapid densification at very low temperatures. However, this activity ceases by about 1050° C, which is only ~35% of the melting point of W[34]. The peak is followed by a decrease in densification rate and a valley in which densification slows by about a factor of two. Then, near 1200°C, the densification rate begins increasing rapidly again. This rise is dramatic and not monotonic: a small peak appears at just below 1250°C, but is quickly followed by a further increase in densification rate until the end of the scan range is reached. Using SEM we see that at 1100°C (Fig. 3d), the interparticle necks have grown more, and, importantly, the phase contrast that we observed as the necks first formed is now missing: the second phase Cr has apparently started to redissolve, or equivalently, W from the particle is dissolving into the Cr-rich necks. At this point,

11

noticeable densification has occurred. However, the material in Figure 3d is still in the initial stages of sintering, as the relative density is still below 70% (cf. Fig. 1). By 1300°C, the necks have grown substantially and the material is apparently predominantly a single phase, with limited discernable phase contrast in Fig. 3e. The larger diameters of the necks in Figure 3e at this point suggest that the material has entered the intermediate sintering stage. After a full scan to 1550°C, a cross-sectional micrograph in Fig. 3f verifies the near full density of the structure.

Thus, the second stage of NPSS, and the one in which most of the densification occurs, is associated with significant chemical redistribution: the phase separation that led to rapid low-temperature neck formation is reversed as the system re-solutionizes. During that process, densification is remarkably accelerated to higher absolute rates than achieved during the initial neck formation. Knowing that these stages exist and are cleanly separable by the peaks in densification rate, we may proceed to analyze their kinetics separately of one another. Our approach is to conduct a Kissinger-style analysis on the critical temperatures associated with those peaks. For a thermally activated process exhibiting a rate maximum during a constant heat rate experiment, Kissinger derived an Arrhenius analysis for the peak temperature to reveal the activation energy [12]. Similar to the MSC, this approach varies the thermal work parameter (in this case the constant heating rate) in order to obtain useful kinetic information. When the Kissinger approach is applied specifically to densification data consistent with the form of Eq. (1), we derive the following Arrhenius analysis[35]:

$$\frac{d\left(\ln\left(\frac{\phi}{T_{peak}}\right)\right)}{d\left(\frac{1}{T_{peak}}\right)} = -\frac{Q}{R} \tag{2}$$

where ϕ is the heating rate, T_{peak} is the temperature of the densification rate peak, Q is the activation energy and R is the universal gas constant. The slope was obtained using linear regression of the

12

experimentally determined $\ln\left(\frac{\phi}{T_{peak}}\right)$ terms, with the error in T_{peak} determined by the data resolution.

The error in the obtained activation energy is the standard error of the linear regression analysis.

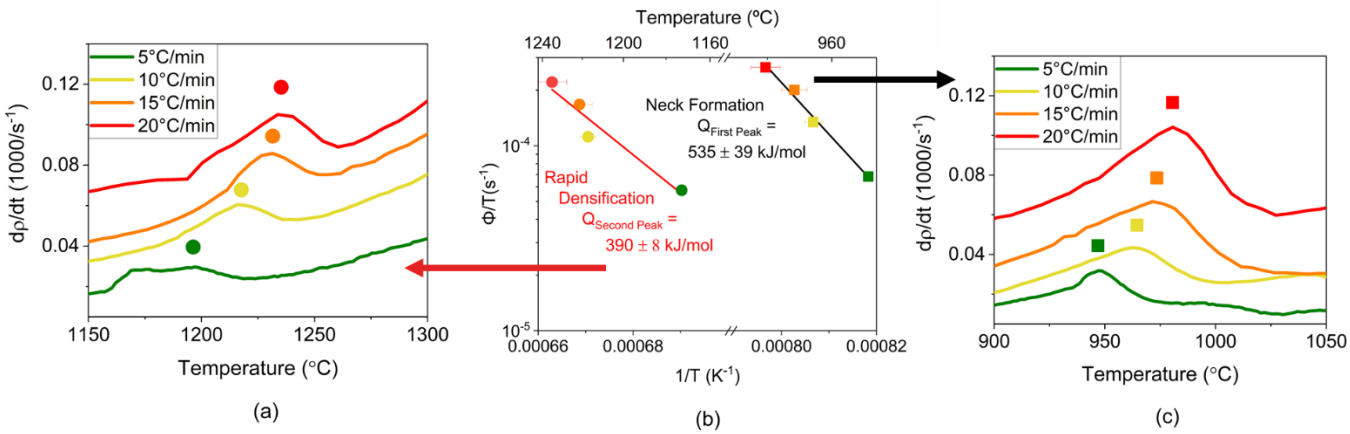

Figure 4: The peak data shown in (a) and (c) are respectively the second and first peaks in the derivative of the data from Fig. 3. The resulting Kissinger-style analysis, shown in (b), shows the activation energies obtained by analyzing the respective peak.

Fig. 4 shows a Kissinger-style analysis following Eq. (2) on the two major densification rate peaks of the W-15Cr system. We begin with an analysis of the second (high-temperature) peak, as it is characteristic of the majority of the densification. The sequence of peaks at different rates is shown in Figure 4a, and their Arrhenius presentation according to the form of Eq. (2) is shown in Figure 4b. The data reasonably conform to the expected Arrhenius scaling, with an activation energy of 390 ± 8 kJ/mol. This value is a good match to the activation energy returned by the master sintering curve analysis (Q = 376 kJ/mol), which is reasonable given that MSC fits the entire densification curve and thus is dominated by the kinetics associated with the most densification; the second peak is associated with most all of the densification (roughly three quarters of the total shrinkage), so its activation energy should indeed be expected to dominate the MSC analysis.

13

This activation energy offers additional insight when it is combined with the microstructural observations in Fig. 3d-f, which show that the densification around the second peak is accompanied by chemical homogenization: the phase separation that led to rapid neck development becomes reversed as W and Cr interdiffuse and recombine into a solid solution, now across the necks. The measured activation energy should therefore reflect the process of interdiffusion between the Cr and W during the homogenization phase. The interdiffusion coefficient for such redissolution is given by Darken's second equation[36]:

$$D_{interdiffusion} = X_A D_{BinA} + X_B D_{AinB} \quad (3)$$

Where the subscripts A and B denote solute and solvent, respectively (in the present example Cr and W respectively). An apparent activation energy from the interdiffusion coefficient in Eq (3) can then be defined as:

$$\frac{d\left(\ln\left(D_{interdiffusion}\right)\right)}{d\left(\frac{1}{T}\right)} = -\frac{Q_{interdiffusion}}{R} \quad (4)$$

Introducing values of D_0= $1.1 \times 10^{-3}\ m^2/s$ and Q = 386 kJ/mol for D_{WinCr}[37] andD_0 = $8.5 \times 10^{-5}\ m^2/s$ and Q = 547 kJ/mol for D_{CrinW} [37]and evaluating $D_{interdiffusion}$ over a range of 1100 to 1550°C, we calculate $Q_{interdiffusion}$ = 386 kJ/mol. We can conclude that interdiffusion is dominated by the diffusion of W in Cr, which has the same value. What is more, this expectation value for the controlling kinetics of the second peak (and the majority of densification in this system) is very well matched by the experimental results for both the MSC (376 kJ/mol) and Kissinger-style analyses (390 kJ/mol) presented earlier. By contrast, the activation energies for self-diffusion (~650 kJ/mol for W and 442 kJ/mol for Cr) are substantially different from the dominant activation energy controlling densification, and can be effectively ruled out as dominant mechanisms of mass transport. Thus, the

14

kinetics of the second densification peak match the assertion that this peak represents the temperature at which densification accelerates and further supports the finding that redissolution of the necks and the associated interdiffusion promotes densification.

Fig. 4c shows the complementary Kissinger analysis on the first, low temperature peak, which our SEM analysis linked to the phase separation and neck formation in NPSS (Fig. 3a-c). Again, the peaks from Fig. 4c convincingly lie on a line in the Arrhenius plot of Fig. 4b, and give an activation energy of 535 ± 39 kJ/mol. This is significantly higher than the values from the second peak (373 kJ/mol) as well as the MSC analysis (376 kJ/mol), which strongly suggests that a different rate limiting process is involved with this stage of sintering. Whereas the low activation energy of 376 kJ/mol seen at high temperatures is characteristic of Cr-like diffusion kinetics, this higher value is suggestive of much more sluggish, W-like kinetics. This is evident in its activation energy being even higher than self-diffusion of Cr (442 kJ/mol). However, it is not as slow as the self-diffusion of W (~650 kJ/mol). Rather, it is a reasonable match for the activation energy for the diffusion of Cr in W, 547 kJ/mol[38]. Because Cr begins in solution in the bulk, it needs to diffuse out of the supersaturated W-Cr particles to form necks; bulk diffusion as a rate limiting step is therefore reasonable. We can envision two pathways by which a Cr atom can travel to the particle surface: 1) through bulk diffusion directly to a free surface or 2) through bulk diffusion to a grain boundary, which provides a short-circuit for subsequent (serial) diffusion to the surface. In either of these cases, the rate-limiting step is bulk diffusion (which aligns with the measured bulk diffusion activation energy), but we can make an estimate of which path is the likely one based on the relative diffusion distances that might be expected in bulk or along grain boundaries, i.e.:

$$\frac{x_{gb}}{x_b} \approx \frac{(D_{gb}t)^{\frac{1}{2}}}{(D_b t)^{\frac{1}{2}}} = \left(\frac{D_{gb}}{D_b}\right)^{\frac{1}{2}} \quad (5)$$

15

where $x_{gb}$and x_b are the boundary and bulk penetration distances respectively, D_{gb} and D_b are the boundary and bulk diffusivities respectively, and t is time. According to Ref [39] we can approximate the grain boundary diffusion using the bulk diffusion parameters. The activation energy of grain boundary diffusion is approximately half of the bulk diffusion activation energy for Cr in W (547 kJ/mol) and the diffusion prefactor for a bcc metal is $1.8 \times 10^{-5}\ m^2/s$. For bulk diffusion of Cr in W, the diffusion prefactor is $8.5 \times 10^{-5}\ m^2/s$ [40].Using these parameter Eq. (5) gives a ratio of ~10^5; diffusion covers many thousands of times more distance along grain boundaries than in the bulk at these times/temperatures. With powder sizes on the order of 1-5 μm in diameter and grain size on the order of 5-20 nm it is clear that it would take longer for an atom to diffuse through the bulk to a grain boundary than from the boundary to the surface. The work of Park et al. [1] on the W-Cr system showed explicitly that the initial nanocrystalline grain size is necessary for accelerated sintering, which corroborates the view that Cr diffuses out of solution to grain boundaries, which then give it rapid access to the powder surface. The above calculations show that even with that being the case, bulk diffusion remains a limiting factor in the serial diffusion process. Therefore, bulk diffusion of Cr in W is the rate limiting step and is what is measured using Kissinger-style analysis.

The above kinetic analyses thus fully conform to a view that the two peaks of NPSS are associated with phase separation at low temperature, and homogenization at high temperature. This conclusion aligns with an examination of the phase diagram for the W-Cr system in Figure 3, upon which we have overlaid the peak positions. The first peak in the derivative curve occurs well within the two phase region[34], as expected since nanophase separation sintering relies on the formation of the secondary phase neck. The position of this peak is not thermodynamic, but kinetic: it appears at the temperature where diffusion is sufficient to achieve phase separation, facilitated by the presence of grain boundaries. After phase separation is complete, there is a large decrease in sintering rate after the first peak, indicating that the mechanism associated with neck building does not lead to sustained

16

densification and is not the primary densification mechanism for the system. The secondary peak, however, occurs during the rapid densification phase and may be more representative of the primary densification pathway of the material. This peak coincides with the point where the W-15Cr samples are expected to transition from a two-phase material to a solid solution on the phase diagram. This aligns with a view that the redissolution of the secondary phase facilitates the accelerated densification observed; the second peak would therefore be thermodynamic in origin and associated with the solubility limit (although it is also diffusional and therefore has kinetic shifts). This observation suggests that third Park criterion (i.e., that the second phase should have a high solubility for the base metal) may be understated; we see that complete redissolution of the necks (100% solubility) appears to be a preferred system characteristic for the fastest densification. We will explore this notion in more detail in other systems below.

17

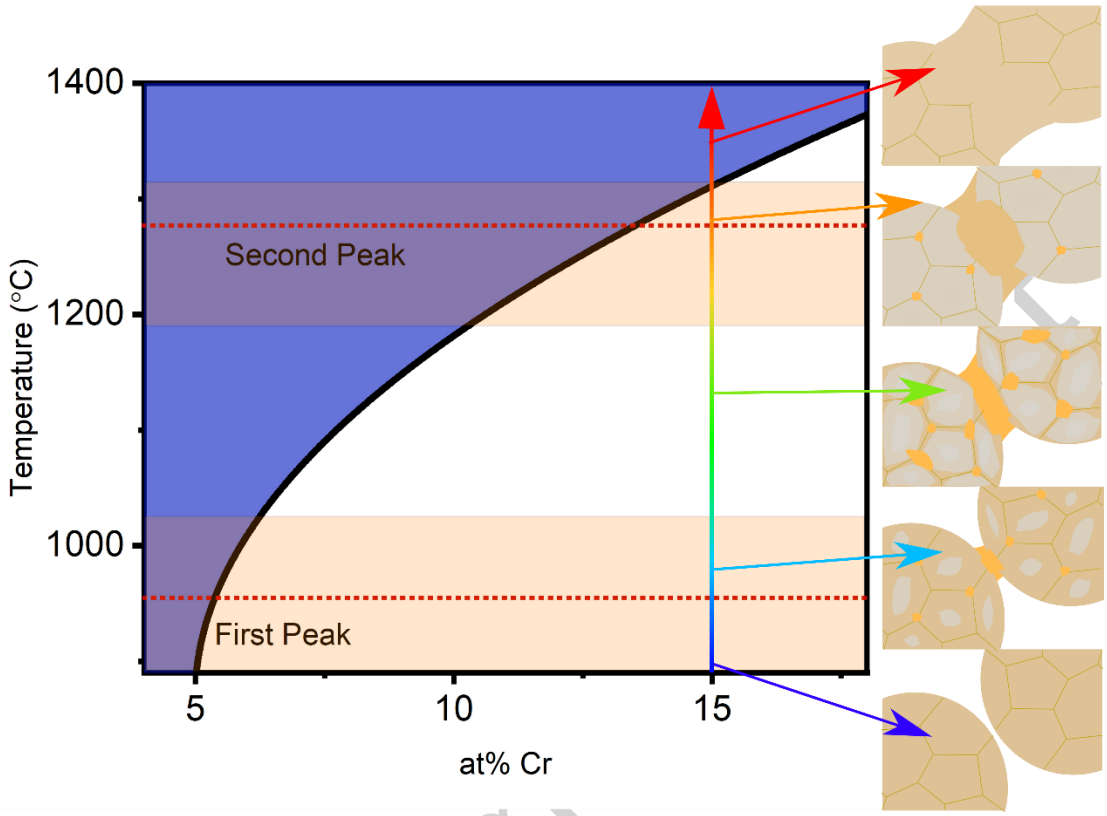

Figure 5: Explanation for the structural evolution during NPSS of the W-15Cr system during a constant heating rate experiment, mapping structural changes schematized at the right to the equilibrium phase diagram.

IV - The Cr-Ni System

The above observations about the two major processes (peaks) in NPSS should be generalizable to other systems to at least some extent, and therefore we proceed to consider the published Cr-Ni system data from Park et al. [2]. We begin with Cr-15Ni dilatometry data shown in in Figure 6a, which exhibits the same type of rapid uptick in densification seen earlier in W-Cr. Close inspection by densification rate analysis again reveals at least two major peaks of activity as seen in Fig. 6b. First, we notice a first peak that occurs near ~600°C, followed by a decrease in densification rate. Then, near 1100°C, the densification rate begins increasing again. During this increase a small second peak appears

18

followed by an increase in densification rate. As shown in Figs. 6c and 6d, those peaks shift with heating rate as expected for Arrhenius processes, with slower scan rates leading to earlier activation. Such peaks are amenable to a Kissinger-style analysis, which is shown in Fig 7a and 7c.

19

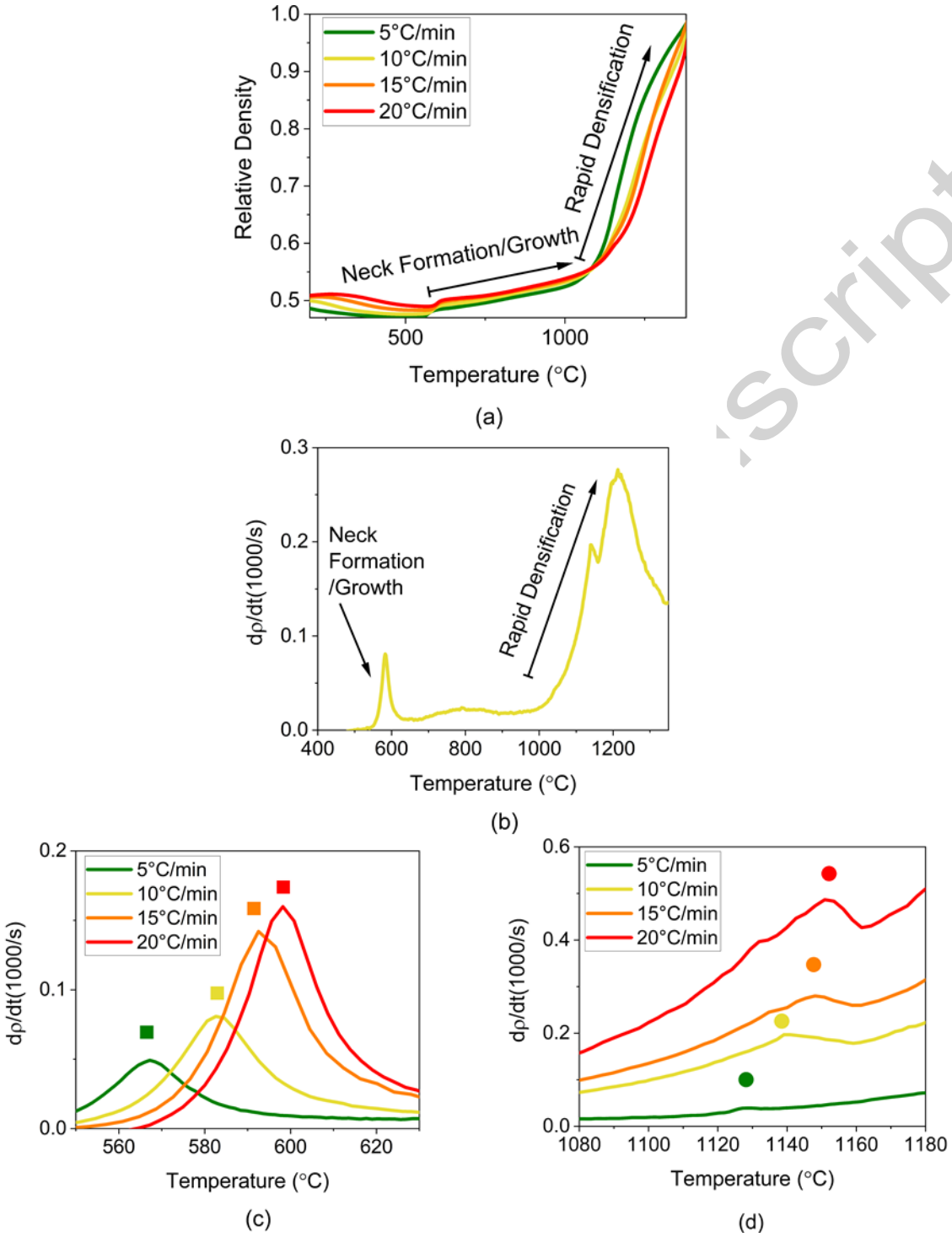

Figure 6: a) densification curves for Cr-15Ni at different heating rates, b) the derivative, densification rate curve for 10°C/min and the c) first and d) second peaks of the derivative curve for all four heating rates

20

Mapping these events to the phase diagram for the Cr-Ni system in Figure 7b, we see that the first peak occurs well within the two phase region[34], just as we saw earlier in the W-Cr system (cf. Fig. 5). This is the range of temperatures where Ni phase separates from Cr, and Park et al. [2] provide images of neck formation in this system that are also analogous to the W-Cr system as we observed in Fig. 3. Again, in this system, there is a decrease in densification rate after the first peak indicating a similar lack of densification resulting solely from neck assembly. The second, high-temperature peak associated with rapid densification coincides with the crossing of the transus from the two-phase region into the solid solution field. This appears to confirm the observations in the previous section for W-Cr, namely, that the redissolution of the necks contributes to the accelerated densification observed. In fact, it is intriguing to note that the greatest accelerated sintering is not noticed until near the edge of the miscibility gap where full dissolution occurs.

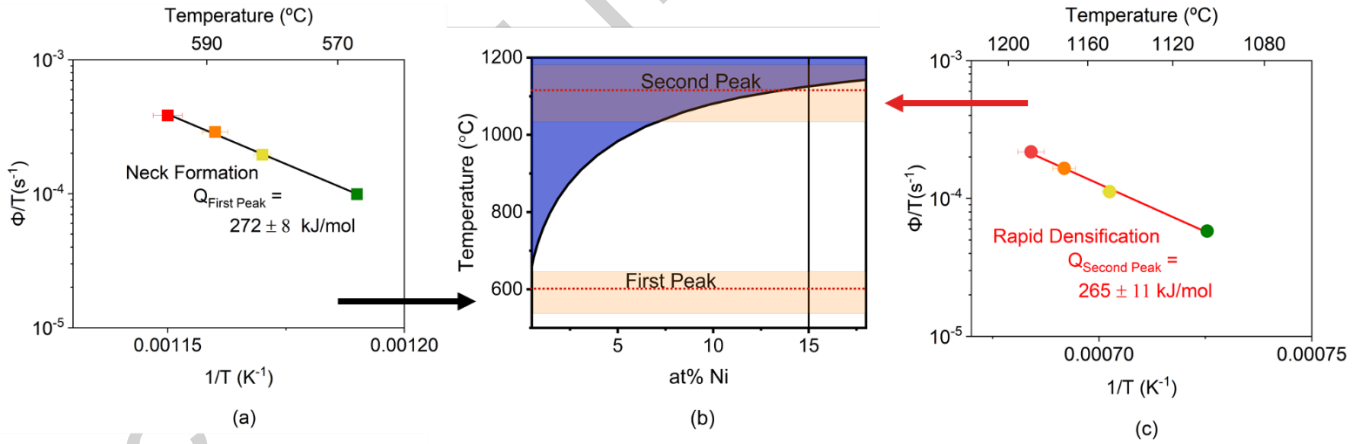

Figure 7: Kissinger analysis for the Cr15Ni derivative curves first (a) and second (c) peaks and their relation to the Cr-Ni phase diagram (b)

The Kissinger-style analysis of these peaks, as seen in Figures 7a and 7c, is also consistent with the mechanistic analysis of the W-Cr system, although in this case due to the kinetic similarities of Cr and Ni, the mechanisms are not easily differentiated by Q alone. The first peak is associated with an activation energy of 272 ± 8 kJ/mol, quite close to the activation energy for the diffusion of Ni in Cr

21

(~280 kJ/mol)[41]. This is consistent with the proposed situation in which Ni needs to diffuse through the bulk of supersaturated Cr-Ni grains to reach grain boundaries, and thereby particle surfaces by short-circuit diffusion. The Kissinger analysis of the second peak gives a slightly lower activation energy of 265 ± 11 kJ/mol. This is similar to the activation energy measured by master sintering curve (265 kJ/mol)[2]. Furthermore, by performing the same interdiffusion analysis using Eqs. (3) and (4) using $D_0 = 1 \times 10^{-4}\ m^2/s$ and Q = 260 kJ/mol for D_{CrinNi} [42] and $D_0 = 1.5 \times 10^{-4}\ m^2/s$ and Q = 280 kJ/mol for D_{NiinCr} [41] over a range of 1000 to 1300°C, we calculate a predicted value for $Q_{interdiffusion}$ = 269 kJ/mol ; the match to the experimental value (265 kJ/mol) is extremely good.

Due to the similarities for the activation energies of diffusion in Cr-Ni, Ni-Cr, and the interdiffusivity between the two phases, it is more difficult to separate the two processes on the basis of Q alone in this system, as compared to the rather stark separation in Q found earlier in the W-Cr system. However, we can perform a second, independent test of the proposed mechanisms by changing the composition in this system; according to the phase diagram in Fig. 8, the redissolution temperature decreases with solute concentration, so a systematic change in densification kinetics around the second peak (but not the first) is expected on this basis.

22

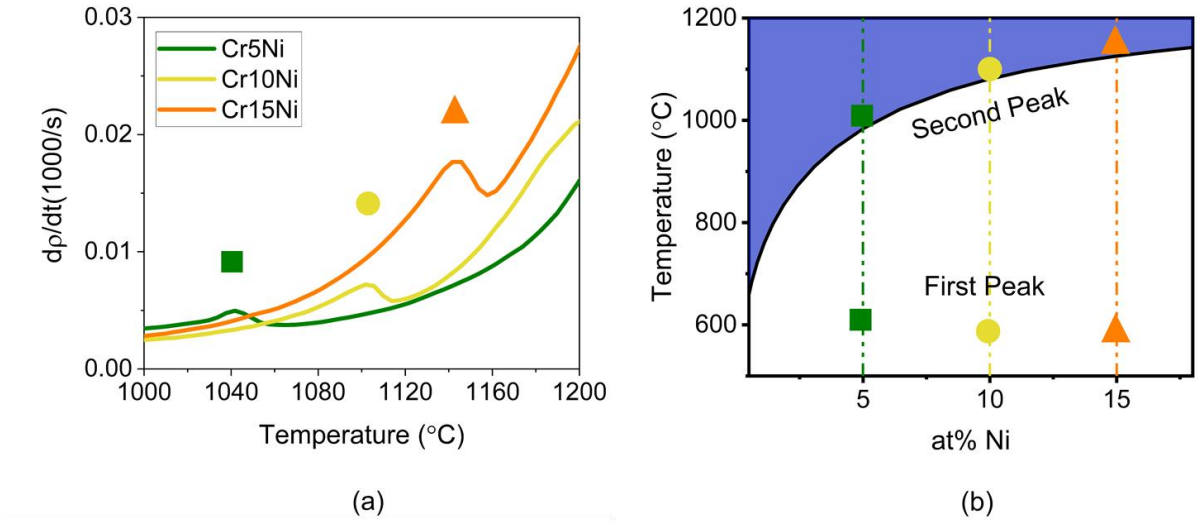

Figure 8:Densification rate curves (a) showing the second (rapid densification) peaks for varying compositions in the Cr-Ni system heated at 10°C/min. Their position on the Cr-Ni phase diagram (b) aligns with the transus, whereas the first peak is essentially independent of composition.

In Fig. 8a we show the secondary peak in densification rate for Cr-5Ni, Cr-10Ni and Cr-15Ni at the same heating rate of 10°C/min. Greater solute (Ni) concentrations lead to higher temperatures for the onset of this peak, and a greater densification signal as well. This is consistent with the proposed view that this peak corresponds to homogenization. As shown in Fig. 8b, these peak positions reasonably match the transition temperatures of the miscibility gap from the phase diagram. This supports the inference that the second peak is thermodynamic and associated with homogenization; the fact that the peak in every case lies slightly above the transus reflects the kinetic nature of the transformation under constant heating rate. Compared to the secondary peak, as also shown in Fig. 8b, the first peak present in Cr-Ni is found to be essentially temperature independent, which also aligns with the suggestion that that peak is not thermodynamic in origin, but kinetically associated with the diffusion of solute out of the bulk.

A point of practical interest here is that in NPSS the temperature for the onset of accelerated densification increases with the amount of solute, according to the solubility curve (Fig. 8). This is

23

opposite to conventional sintering acceleration techniques, which require greater additions in order to obtain faster/more complete densification[43–48]. For example, other acceleration mechanisms rely on rearrangement (facilitated by a liquid phase) of particles, or rapid diffusion through a permanent secondary phase (liquid or solid)[4,43], mechanisms that are enhanced by greater solute concentration. Based on the present analysis of NPSS in both the W-Cr and Cr-Ni systems, redissolution and loss of the second phase is a critical event for this accelerated sintering mechanism, rather than any processes involving the secondary phase directly. Thus, because redissolution occurs at lower temperatures for lower solute concentrations, so does accelerated densification. The practical implications of this require greater exploration, but it is encouraging that the greatest sintering acceleration may occur at low solute additions.

V - The Ti-Mg System

As noted in the Introduction, the Ti-Mg system is one that was studied as a test case of the Park NPSS criteria, because it met the first two of these but not the third; that system exhibits immiscibility and the additive (Mg) has a lower melting point than the base metal (Ti), but at no temperature is there significant solubility of Ti in Mg[49]. Our analysis above suggests that the third criterion is not only important to NPSS, it is in fact understated: we find the most acceleration not just when there is some solubility of the components, but when they fully homogenize into a solid solution. In what follows, then, we analyze the published data of Graetz et al. [18] on Ti-Mg, which is replotted in Fig. 9a.

When analyzing the derivatives of the densification curves for the Ti-20Mg samples a single peak was observed in Figure 9b, occurring at ~510°C. Unlike the W-Cr and Cr-Ni systems, the Ti-Mg system does not have any significant temperature ranges where the Ti-20Mg will form a solid solution as in evident in the phase diagram in Figure 9c [49].

24

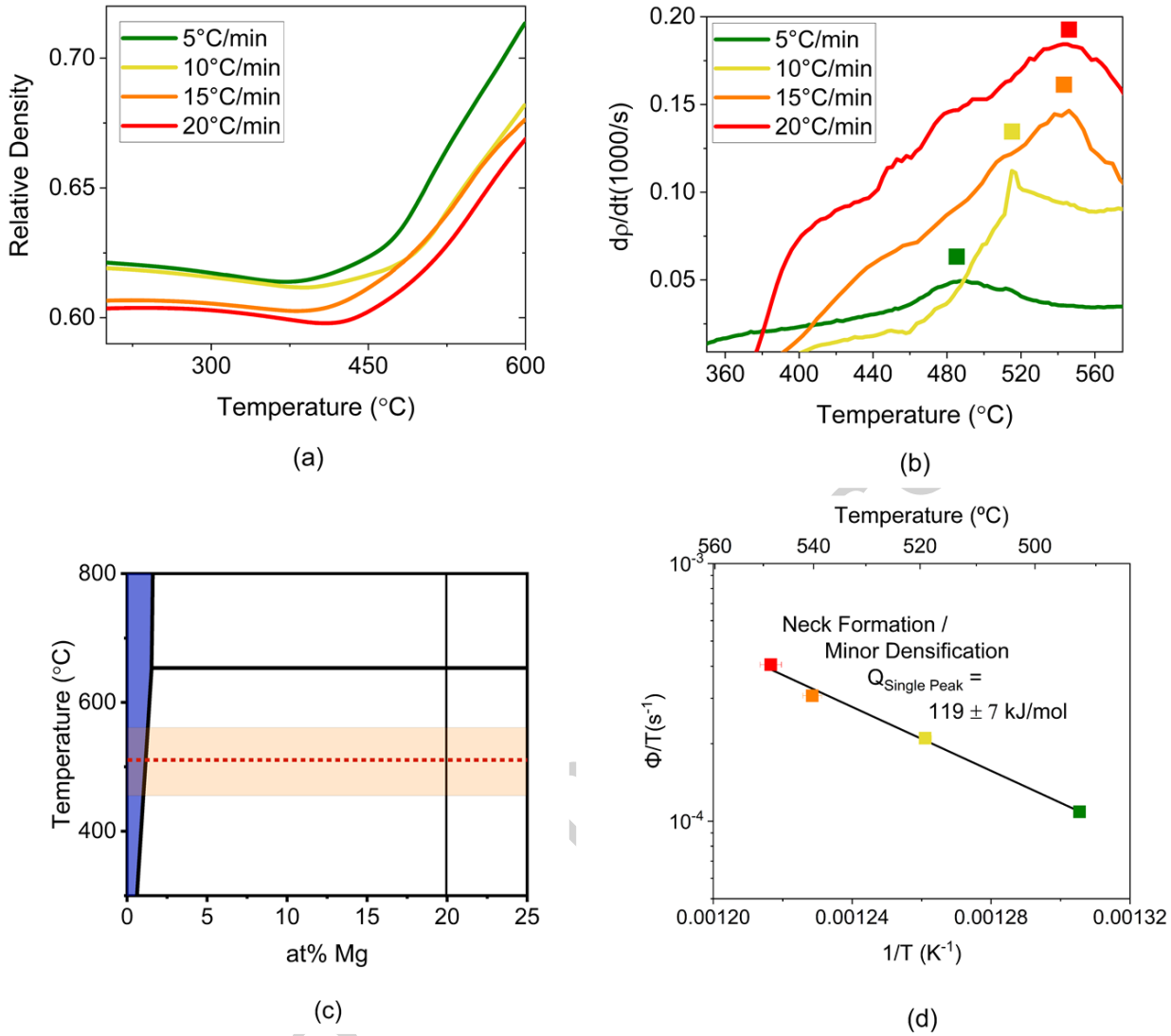

Figure 9:Densification (a) and densification rate (b) curves for Ti-20Mg the position of the peak on the equilibrium phase diagram (c), and their Kissinger analysis (d)

Performing a Kissinger analysis on this singular peak, as seen in Fig 9d, yields an activation energy of 119 ± 7 kJ/mol. This activation energy does not correspond to the bulk diffusion of titanium (169 kJ/mol)[38], nor to the diffusion of Ti in Mg at 201 kJ/mol[50]. It is closer to that for the self-diffusion of Mg (135 kJ/mol)[38]. We are not aware of data for bulk diffusion of Mg through Ti, but it would almost certainly be closer to the latter value and characteristic of Mg-like diffusion kinetics, and thus might well match the measured value from Fig. 9 at 119 kJ/mol. This would imply that these experiments achieve

25

just the first stage of NPSS, which involves only a minor contribution to densification. This can explain why this system does not achieve full density generally; although the first peak appears and second phase necks are assembled, the Ti-20Mg alloy composition does not cross from a two-phase region to a solid solution region like the W-Cr and Cr-Ni systems. This result thus further supports the importance of the formation of the solid solution for the full densification of the material. Without the formation of the solid solution, no interdiffusion occurs that would facilitate the rapid solid-state densification.

VI - Conclusion

In order to better understand and optimize nano phase-separation sintering (NPSS) it is necessary to better understand the sequence of mechanisms leading to structural evolution and complete densification. While a master sintering curve (MSC) analysis helps determine the average kinetics of accelerated sintering, it does not separate the various mechanisms necessary for NPSS, and does not provide information about the critical temperature ranges where those various mechanisms are important. To better analyze these systems, we have introduced a Kissinger-style kinetic analysis on the derivative of the densification curves during NPSS. This analysis reveals two critical mechanisms during the sintering process.

First, at low temperatures in the miscibility gap, phase separation occurs at a temperature that is governed by system kinetics. Solute diffuses through the bulk, which is the rate-limiting kinetic step, as it finds grain boundaries and particle surfaces. The net result of this low temperature process is the assembly of second phase necks between powder particles. The formation and growth of these necks is not the most important densifying mechanism, and its kinetics are characterized by the very high

26

activation energy of solute diffusion in the base metal lattice. The function of this stage is to assemble interparticle necks, which do play a critical role in densification later, by a different mechanism.

Second, at high temperatures, densification accelerates dramatically when the solubility limit for the second phases is reached, and the two elements are free to fully interdiffuse. As the transus is crossed, we observe full homongenization of the alloy, across interparticle necks. The kinetic signature of the rapid densification that sets on there is quantitatively associated with interdiffusion. The third criterion previously suggested for successful NPSS is a high solubility of base metal in solute, so that the interparticle necks can transport matter and efficiently promote densification. The present results more quantitatively show that not just a high solubility, but rather full solubility (full solutionization) is desired. In the Cr-Ni system we established this criterion at several compositions, showing the crossing of the solubility curve is indeed limiting to the process of NPSS, while in the Ti-Mg system the lack of full solubility suppresses the rapid densification seen in other systems.

Such kinetic insights on structural evolution help to narrow the design space for NPSS alloys, and also point to concepts for the design of optimal pressureless sintering treatment for conventional and additive manufacturing techniques, to obtain a fully densified material at the lowest possible temperatures. For example, it is anomalous that lower concentrations of solute appear useful to accelerate NPSS, when typically, accelerated sintering schemes involve the use of greater additive contents to achieve faster sintering; this concept represents an interesting direction for future work.

Acknowledgements

This work was supported by the National Aeronautics and Space Administration under grants No. 80NSSC19K1055 and 029856-00001 and made use of the MRSEC Shared Experimental Facilities at MIT, supported by the National Science Foundation under award number DMR-1419807.

Conflict of Interest

Christian Oliver and Christopher A. Schuh are both affiliated with Massachusetts Institute of Technology. Massachusetts Institute of Technology has licensed patents and submitted patent applications for nanophase separation sintering alloys including for material systems discussed in these results.

28

VII - References

1 M. Park and C.A. Schuh: *Nat. Commun.*, DOI:10.1038/ncomms7858.
2 M. Park, T. Chookajorn, and C.A. Schuh: *Acta Mater.*, 2018, vol. 145, pp. 123–33.
3 R.M. German: *Sintering Theory and Practice*, John Wiley & Sons, 1996.
4 R.M. German: *Liquid Phase Sintering*, Springer Science & Business Media, 2013.
5 P.K. Samal and J.W. Newkirk: in *ASM Handbook,Volume 07 - Powder Metallurgy*, ASM International.
6 R.M. German: *Metall. Mater. Trans. A*, 1997, vol. 28, pp. 1553–67.
7 C. Padmavathi and A. Upadhyaya: *Sci. Sinter.*, 2010, vol. 42, pp. 363–82.
8 Z.Z. Fang: *Sintering of Advanced Materials*, Elsevier, 2010.
9 J.L. Johnson and R.M. German: *Metall. Mater. Trans. B*, 1996, vol. 27, pp. 901–9.
10 J.L. Johnson and R.M. German: *Metall. Trans. A*, 1993, vol. 24, pp. 2369–77.
11 A. Upadhyaya and R.M. German: *Metall. Mater. Trans. A*, 1998, vol. 29, pp. 2631–8.
12 J. Liu, A. Lal, and R.M. German: *Acta Mater.*, 1999, vol. 47, pp. 4615–26.
13 A. Bose, C.A. Schuh, J.C. Tobia, N. Tuncer, N.M. Mykulowycz, A. Preston, A.C. Barbati, B. Kernan, M.A. Gibson, D. Krause, T. Brzezinski, J. Schroers, R. Fulop, J.S. Myerberg, M. Sowerbutts, Y.-M. Chiang, A. John Hart, E.M. Sachs, E.E. Lomeli, and A.C. Lund: *Int. J. Refract. Met. Hard Mater.*, 2018, vol. 73, pp. 22–8.
14 R. Raman and R.M. German: *Metall. Mater. Trans. A*, 1995, vol. 26, pp. 1909–1909.
15 P. Nandwana, A.M. Elliott, D. Siddel, A. Merriman, W.H. Peter, and S.S. Babu: *Curr. Opin. Solid State Mater. Sci.*, 2017, vol. 21, pp. 207–18.
16 A. Bose, A. Lund, J. Reidy, C. Craven, M. Gibson, A. Barbati, C. Schuh, L. Jorgensen, J. Tobia, A. Dias, and N. Tuncer: *Int. J. Powder Metall.*
17 N. Azgomi, F. Tetteh, S.H. Duntu, and S. Boakye-Yiadom: *Metall. Mater. Trans. A*, 2021, vol. 52, pp. 3382–400.
18 K. Graetz, J.S. Paras, and C.A. Schuh: *Materialia*, 2018, vol. 1, pp. 89–98.
19 H. Su and D.L. Johnson: *J. Am. Ceram. Soc.*, 1996, vol. 79, pp. 3211–7.
20 D. Blaine, J. Gurosik, S.J. Park, and D. Heaney: *Metall. Mater. Trans. A*, 2006, vol. 37, pp. 715–20.
21 M. Vattur Sundaram, K.B. Surreddi, E. Hryha, A. Veiga, S. Berg, F. Castro, and L. Nyborg: *Metall. Mater. Trans. A*, 2018, vol. 49, pp. 255–63.
22 J. Banerjee, A. Ray, A. Kumar, and S. Banerjee: *J. Nucl. Mater.*, 2013, vol. 443, pp. 467–78.
23 D.C. Jana, G. Sundararajan, and K. Chattopadhyay: *Metall. Mater. Trans. A*, 2018, vol. 49, pp. 5599–606.
24 I.M. Robertson and G.B. Schaffer: *Metall. Mater. Trans. A*, 2009, vol. 40, pp. 1968–79.
25 S.J. Park, S.H. Chung, J.M. Martín, J.L. Johnson, and R.M. German: *Metall. Mater. Trans. A*, 2008, vol. 39, pp. 2941–8.
26 T. Frueh, I.O. Ozer, S.F. Poterala, H. Lee, E.R. Kupp, C. Compson, J. Atria, and G.L. Messing: *J. Eur. Ceram. Soc.*, 2018, vol. 38, pp. 1030–7.
27 D.L. Johnson: *Charact. Model. Control Sintered Ceram. Microstruct. Prop.*, 2006, pp. 1–13.
28 V. Pouchly, K. Maca, and Z. Shen: *J. Eur. Ceram. Soc.*, 2013, vol. 33, pp. 2275–83.
29 *Standard Practices for Production and Preparation of Powder Metallurgy (PM) Test Specimens*, .
30 *Standard Test Method for Linear Thermal Expansion of Solid Materials by Thermomechanical Analysis*, .

29

31 S. Solonin, Y.M. Solonin, and V. Skorokhod: *Sov. Powder Metall. Met. Ceram.*, 1966, vol. 5, pp. 782–8.
32 M. Park: PhD Thesis, Massachusetts Institute of Technology, 2015.
33 R. Koc and S.K. Kodambaka: *J. Eur. Ceram. Soc.*, 2000, vol. 20, pp. 1859–69.
34 P.E.A. Turchi, L. Kaufman, and Z.-K. Liu: *Calphad*, 2006, vol. 30, pp. 70–87.
35 C. Oliver and C.A. Schuh: *Metall. Mater. Trans. A*, DOI:10.1007/s11661-021-06399-y.
36 L.S. Darken: *Trans Aime*, 1948, vol. 175, pp. 184–201.
37 M. Park, K.C. Alexander, and C.A. Schuh: *J. Alloys Compd.*, 2014, vol. 611, pp. 433–9.
38 W.F. Gale and T.C. Totemeier: in *Smithells Metals Reference Book (8th Edition)*, Elsevier.
39 C. Herzig and Y. Mishin: in *Diffusion in Condensed Matter: Methods, Materials, Models*, 2005, pp. 337–66.
40 S. Klotsman, V.M. Koloskov, S. Osetrov, I. Polikarpova, G. Tatarinova, and A. Timofeyev: vol. 66, Trans Tech Publ, 1990, pp. 439–46.
41 W.F. Gale and T.C. Totemeier: in *Smithells Metals Reference Book (8th Edition)*, Elsevier.
42 J. Askill: *Phys. Status Solidi A*, 1971, vol. 8, pp. 587–96.
43 R. German: *Sintering Theory and Practice*, .
44 D. Takahata, W.A. Miller, and K.T. Aust: *Metall. Trans. A*, 1978, vol. 9, pp. 935–40.
45 Y.F. Yang, S.D. Luo, C.J. Bettles, G.B. Schaffer, and M. Qian: *Mater. Sci. Eng. A*, 2011, vol. 528, pp. 7381–7.
46 W. Wei, Y. Liu, K. Zhou, and B. Huang: *Powder Metall.*, 2003, vol. 46, pp. 246–50.
47 I.M. Robertson and G.B. Schaffer: *Powder Metall.*, 2009, vol. 52, pp. 311–5.
48 D.Q. Zhang, Z.H. Liu, Q.Z. Cai, J.H. Liu, and C.K. Chua: *Int. J. Refract. Met. Hard Mater.*, 2014, vol. 45, pp. 15–22.
49 J.L. Murray: *Bull. Alloy Phase Diagr.*, 1986, vol. 7, pp. 245–8.
50 B.-C. Zhou, S.-L. Shang, Y. Wang, and Z.-K. Liu: *Data Brief*, 2015, vol. 5, pp. 900–12.

30